

PAPER

Ta, Ti and Hf effects on Nb₃Sn high-field performance: temperature-dependent dopant occupancy and failure of Kramer extrapolation

To cite this article: Chiara Tarantini *et al* 2019 *Supercond. Sci. Technol.* **32** 124003

View the [article online](#) for updates and enhancements.







IOP | ebooks™

Bringing you innovative digital publishing with leading voices to create your essential collection of books in STEM research.

Start exploring the collection - download the first chapter of every title for free.

Ta, Ti and Hf effects on Nb₃Sn high-field performance: temperature-dependent dopant occupancy and failure of Kramer extrapolation

Chiara Tarantini¹ , Shreyas Balachandran¹ , Steve M Heald², Peter J Lee¹ , Nawaraj Paudel¹, Eun Sang Choi¹, William L Starch¹ and David C Larbalestier¹ 

¹ National High Magnetic Field Laboratory, Florida State University, Tallahassee, FL 32310, United States of America

² Advanced Photon Source, Argonne National Laboratory, Argonne, IL 60439, United States of America

E-mail: tarantini@asc.magnet.fsu.edu

Received 7 August 2019, revised 20 September 2019

Accepted for publication 14 October 2019

Published 4 November 2019



CrossMark

Abstract

The increasing demand for improving the high-field (16–22 T) performance of Nb₃Sn conductors requires a better understanding of the properties of modern wires much closer to irreversibility field, H_{Irr} . In this study we investigated the impact of Ta, Ti and Hf doping on the high-field pinning properties, the upper critical field, H_{c2} , and H_{Irr} . We found that the pinning force curves of commercial Ti and Ta doped wires at different temperatures do not scale and that the Kramer extrapolation from low field data, typically used by magnet designers to estimate high-field critical current density and magnet operational margins, is not reliable and significantly overestimates the actual H_{Irr} . In contrast, new laboratory scale conductors made with Nb–Ta–Hf alloy have improved high-field J_c performance and, despite contributions by both grain boundary and point defect pinning mechanisms, have more predictable high-field behavior. Using Extended x-ray Absorption Fine Structure spectroscopy, EXAFS, we found that for the commercial Ta and Ti doped conductors, the Ta site occupancy in the A15 structure gradually changes with the heat treatment temperature whereas Ti is always located on the Nb site with clear consequences for H_{c2} . This work reveals the still limited understanding of what determines H_{c2} , H_{Irr} and the high-field J_c performance of Nb₃Sn and the complexity of optimizing these conductors so that they can reach their full potential for high-field applications.

Keywords: Nb₃Sn, EXAFS, site occupancy, irreversibility field, Kramer's extrapolation, pinning mechanisms

(Some figures may appear in colour only in the online journal)

1. Introduction

Nb₃Sn provides the most technologically ready conductors for the realization of high field accelerator magnets beyond the limits of Nb–Ti. In fact, Nb₃Sn has been selected for the magnets employed in the Hi-Luminosity upgrade of the Large Hadron Collider [1–3] and it is the first choice for the realization of the Future Circular Collider [4]. Because of the very

demanding requirements of this project and broad interest in improving the performance for other applications like NMR spectroscopy, compact cyclotrons and magnetically confined fusion reactors, a better understanding of the limits of present commercially available conductor could provide insights for further improvements or development of new conductor designs. Because of the need to enhance the high field properties, investigation of pinning mechanisms and the

variation of the irreversibility field, H_{Irr} , and the upper critical field, H_{c2} , are of great interest.

Historically the main vortex pinning mechanism considered responsible for Nb₃Sn properties is grain boundary (GB) pinning whose functional dependence is given by $F_{p,GB}(H) = A_{GB} \left(\frac{H}{H_{Irr}} \right)^{0.5} \left(1 - \frac{H}{H_{Irr}} \right)^2$ [5–8]. Since the H_{Irr} of Nb₃Sn conductors (~23–25 T) greatly exceeds the typical fields (~15 T) available in most laboratories, H_{Irr} is typically estimated by extrapolation from mid-field data using the Kramer function $Kr(H) = J_c^{0.5} (\mu_0 H)^{0.25}$ [9]. In fact the $Kr(H)$ function corresponds to the linearization of the $F_{p,GB}(H)$ function with H_{Irr} defined as $Kr = 0$. Indeed a valuable correlation was found by the US Magnet Development Program between this H_{Irr} extrapolation and the I_c (4.2 K, 15 T) performance of conductors, even though they assumed the same field-dependent $f_p(h)$ function to be valid at every temperature (with f_p and h being the reduced- F_p and H/H_{Irr}) and employed it to estimate the operational margin [10]. Previous high-field measurements on Nb₃Sn wires showed good temperature scaling for the F_p curves and roughly linear trends for the Kramer function. However, some deviations from the Kramer function near H_{Irr} were also previously observed and they were attributed to compositional inhomogeneities (see [8, 11] and references within). However, the validity of the Kramer extrapolations as a means to predict $J_c(H, T)$ outside the 15 T range has not been experimentally verified at high fields in modern Ta/Ti-doped Nb₃Sn conductors where the dopants are invariably used to increase H_{Irr} and H_{c2} .

Another area of interest is the recent discovery that the Nb₃Sn vortex pinning properties can be strongly modified in wires at high fields by introducing group IVB dopants, such as Zr or Hf, together with Ta [12]. Although Zr and Hf were already used in the early 80s and 90s to improve Nb₃Sn performance [13–17] now they are employed to enhance the pinning force density, F_p , alongside Ta, which keeps H_{Irr} close to the values of commercial conductors. This approach led to an increase in the bulk pinning force maximum from values that are typically ~4.6 T to values over 5.8 T (at 4.2 K) and an improvement by a factor three in the layer critical current density at 4.2 K and 16 T for the Hf-doped wire without the need for internal oxidation by using SnO₂ (SnO₂ appears to be necessary in the Zr case). Avoidance of SnO₂ is particularly appealing for wire manufacturers because it would allow a more straightforward transition from lab-scale to commercial fabrication. Interestingly, pinning force measurements on the Hf and Zr wires indicate a strong contribution to pinning from a source other than grain boundaries, most likely point defects (PD), as inferred by the significant shift toward higher field of the F_p maximum, despite small variation of H_{Irr} . The high irreversibility field of oxidized Ta-Zr doped laboratory-scale monofilaments was also confirmed by simultaneous work conducted on multifilamentary wires [18]. For future use of these newly alloyed wires, a better understanding of how to analyze and to predict their behavior would be valuable.

As mentioned above, Ta and/or Ti are the H_{c2} -enhancing dopants used in current Nb₃Sn production strand, and we may recall that, in bronze wires, Ta appeared to be only half as efficient as Ti maximizing H_{c2} , since it requires ~4 at%Ta while less than 2 at%Ti is needed [17]. For many years they both were assumed to occupy the Nb site in the A15 structure [19–21]. However, analyzing the overall A15 layer compositions and noticing the frequent Sn deficiency (<25%) in Ti-doped Nb₃Sn compared to the Ta case, it was suggested that Ta occupies the Nb site whereas Ti the Sn site [22]. To test this hypothesis, we employed EXAFS (Extended x-ray Absorption Fine Structure), which much to our surprise showed that Ti actually sits only on the Nb site, whereas Ta splits between the Nb and Sn sites [23]. This finding revealed that H_{c2} is not simply determined by the dopant itself but also by the anti-site disorder (i.e. Nb on the Sn site and vice versa) that the dopant induces. Moreover, since a sensibly different overall composition and site occupancy were found in two different Ta-doped conductors (a 54/61 and a 108/127 restack designs with ~50 and 70 μm filament diameter, respectively) after different heat treatments (HTs), a possible effect of the HT on site occupancy was hypothesized.

In this work we explore some of these ideas. By high-field characterization we investigate the temperature dependence of F_p for a modern RRP[®] conductor to verify whether or not the Kramer extrapolation is a reliable way to determine H_{Irr} and whether the GB functional dependence can be assumed at all temperatures. The same type of characterization was also employed to investigate how the pinning mechanisms change in Zr and Hf-alloyed conductors. We also suggest how to estimate H_{Irr} when it is not possible to access high-field facilities. Finally we heat treated Ta and Ti-doped RRP[®] Nb₃Sn wires and used EXAFS to see whether or not the site occupancy changes with HT temperature. With these results and with specific heat characterization, the effects on H_{c2} are also discussed.

2. Experimental

In this work we characterize both commercial multifilamentary strands and laboratory-scale monofilaments. First we studied two 0.82–0.85 mm diameter, 108/127 design large-scale production RRP[®] strands: a standard-Sn Ta-doped wire, heat treated at 634 °C, 666 °C and 711 °C for 48 h, and a reduced-Sn Ti-doped wire, heat treated for 48 h at 5 different temperatures between 606 °C and 727 °C. The second sample type employed monofilamentary wires made with three different alloys: Nb-4Ta, Nb-4Ta1Zr and Nb-4Ta1Hf by atomic percent. Each of these alloys was employed in wires made with two different Cu–Sn powder mixtures, one with and one without SnO₂, as described in [12]. These special alloyed wires underwent a 670 °C/100 h A15 reaction. The best performing of these wires used a Ta–Hf alloy without SnO₂ and is the primary focus here. Figure 1 shows the field emission scanning electron microscope images of the two RRP strands and of the Ta–Hf monofilamentary wire.

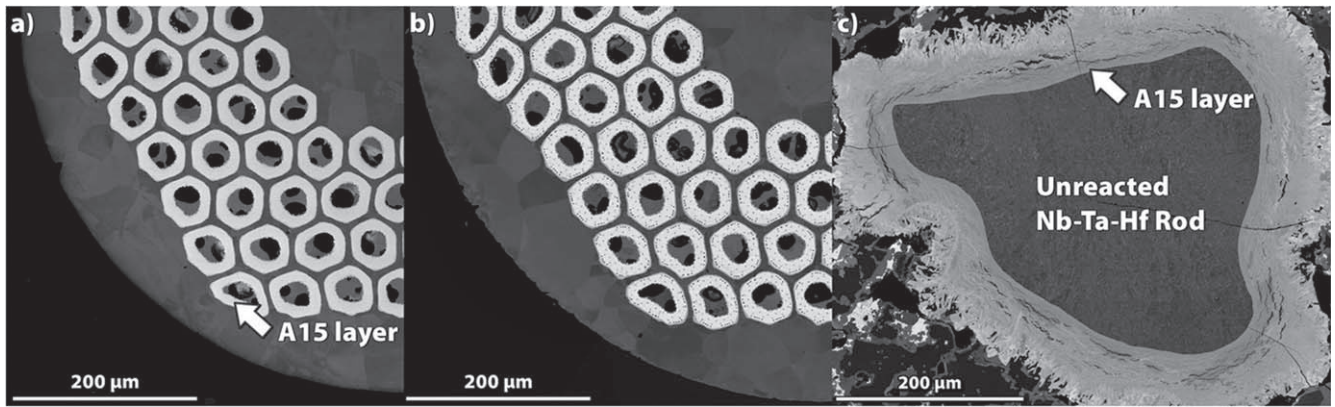


Figure 1. FESEM backscattered electron images showing partial cross-sections of (a) the Ta-doped RRP-13711 (48 h/664 °C) wire, (b) the Ti-doped RRP-149984 (48 h/665 °C) wire and (c) the monofilamentary Ta and Hf doped wire.

Magnetization hysteresis loops were performed in two vibrating sample magnetometers (VSM), one mounted in a 14 T superconducting magnet and one in the 35 T resistive magnet at the National High Magnetic Field Laboratory so as to enable the pinning force curves to be determined. To avoid the difficulties of determining *a priori* the irreversibility field H_{Irr} to investigate the F_p curves and to compare the shape with the expected theoretical trends, here we prefer to normalize the applied field H to the position of the maximum, H_{Max} , obtaining the F_p/F_{pMax} versus H/H_{Max} plots (instead of the more commonly employed F_p/F_{pMax} versus H/H_{Irr}). With this normalization the theoretical GB and PD curves go to zero at $H/H_{Max} = 5$ and 3, respectively (dashed lines in figure 2(b)) [24].

EXAFS characterization occurs at x-ray energies above the absorption edge energy of the element under investigation. By tuning the x-ray energy to different absorption edges (like for Ta or Ti), the local structure surrounding specific elements in a complex material can be resolved. The measurements were made on beamline 20-ID at the Advanced Photon Source. More details can be found in [23].

Specific heat characterizations were also performed in a 16 T Quantum Design physical property measurement system to determine H_{c2} of selected wires as described in [25] and [26].

3. Results

3.1. VSM characterization and analysis of commercial RRP[®] multifilamentary wire

The hysteresis loops of the Ta-doped RRP[®] wires were obtained in high magnetic fields. The F_p curves of the sample heat treated at 666 °C were estimated in the 3–14 K range and are reported in figure 2(a) as well as the same curves normalized to the peak position of F_p in figure 2(b). These plots reveal that the F_p curves do not scale and that all high temperature data clearly exceed the GB function in the high field region. Only at 3 K do the data approach the GB function but there are still evident deviations.

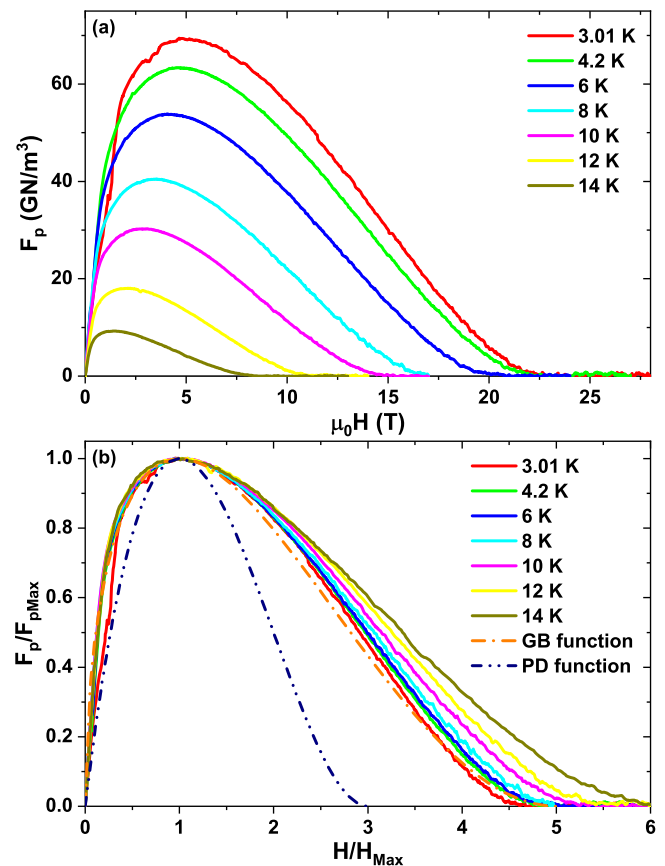


Figure 2. (a) Field dependence of the non-Cu F_p at different temperatures and (b) the same curves normalized to maximum for a Ta-doped RRP[®] wire. The dashed lines represent the theoretical function for grain boundary (GB) and point defect (PD) pinning mechanisms.

As explained in the introduction, the typical method to analyze the superconducting properties is to use the Kramer plot $Kr(H) = J_c^{0.5}(\mu_0 H)^{0.25}$. Figure 3 reports these curves to verify the deviation from linearity of $Kr(H)$ and to estimate how much this affects the H_{Irr} estimation. The main panel shows that the Kramer plots have marked upward curvatures at low fields (just above the maximum) and high temperatures, whereas at low temperature there are two opposite

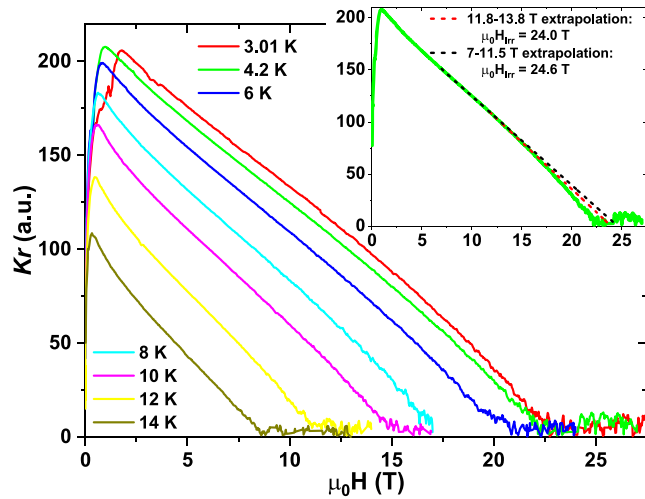


Figure 3. Kramer plots at different temperatures for a Ta-doped RRP[®] wire. In the inset the 4.2 K data with extrapolations over different ranges (see main text).

curvatures: upward in the low field region (below $\sim 1/3H_{Irr}$) and downward curvature in the high field region (from $\sim 1/3H_{Irr}$ to almost H_{Irr}). The field-range employed for the extrapolation to determine H_{Irr} usually depends on the magnet available. A few examples are shown in the inset of figure 3 for the 4.2 K curve. In our laboratory a 14 T VSM is routinely used for the wire characterization and, with a 11.8–13.8 T extrapolation range, a $\mu_0 H_{Irr} \sim 24$ T would be estimated. Transport characterization frequently relies on smaller magnets [27] and a 7–11.5 T extrapolation leads to $\mu_0 H_{Irr} \sim 24.6$ T. However, the present high-field characterization shows that the actual $\mu_0 H_{Irr}$ is about 22.4 T. This means that the mid-field extrapolations noticeably overestimate H_{Irr} by more than 2 T (further analysis is given in section 4).

Since we previously demonstrated that Ta-doped wires tend to have a larger distribution of properties than Ti-doped ones [28], we also investigated by VSM a similarly heat-treated Ti-doped RRP[®] wire. The trend was overall the same of figure 2(b) thus assuring us that these nonlinear Kramer plot are not simply due to inhomogeneity of the Nb₃Sn phase.

3.2. VSM characterization and analysis of special alloyed monofilamentary wire

Similar characterization was performed on the high- J_c monofilamentary wires prepared with special alloys. Figure 4 shows the data for the wire manufactured with Nb–Ta–Hf alloy (without the use of SnO₂). It can be seen that also in this case there is a clear temperature dependence of the shape of the pinning force. However, differently from the RRP[®] samples, the normalized curves mostly lie between the GB and the PD functions suggesting a mixed contribution of those pinning mechanisms. In this case the Kramer plots (figure 5) show a obvious downward curvature on substantially the entire field range. This means that, for these

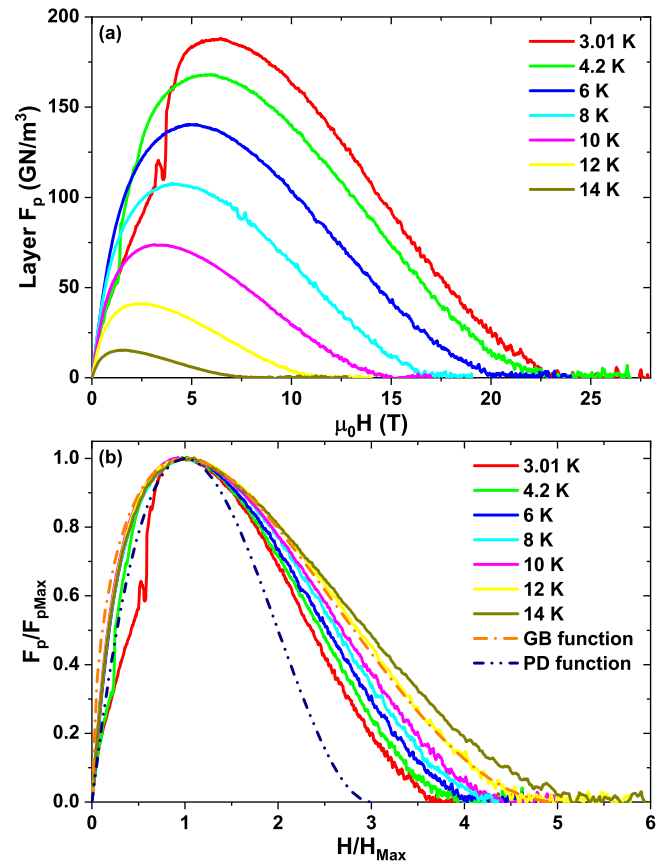


Figure 4. (a) Field dependence of the layer F_p at different temperatures and (b) the same curves normalized to the maximum for a Ta–Hf-doped monofilamentary wire (low-field, low-temperature data affected by flux jumps). The dashed lines represent the theoretical function for grain boundary (GB) and point defect (PD) pinning mechanisms.

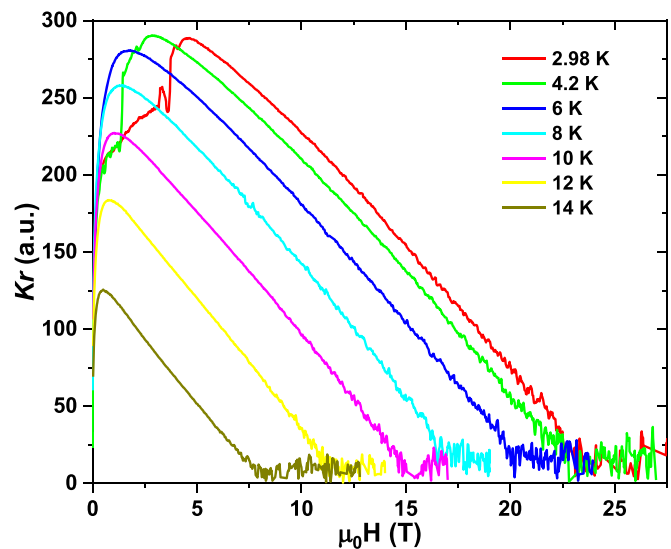


Figure 5. Kramer plots at different temperatures for a high- J_c Ta–Hf-doped monofilamentary wire.

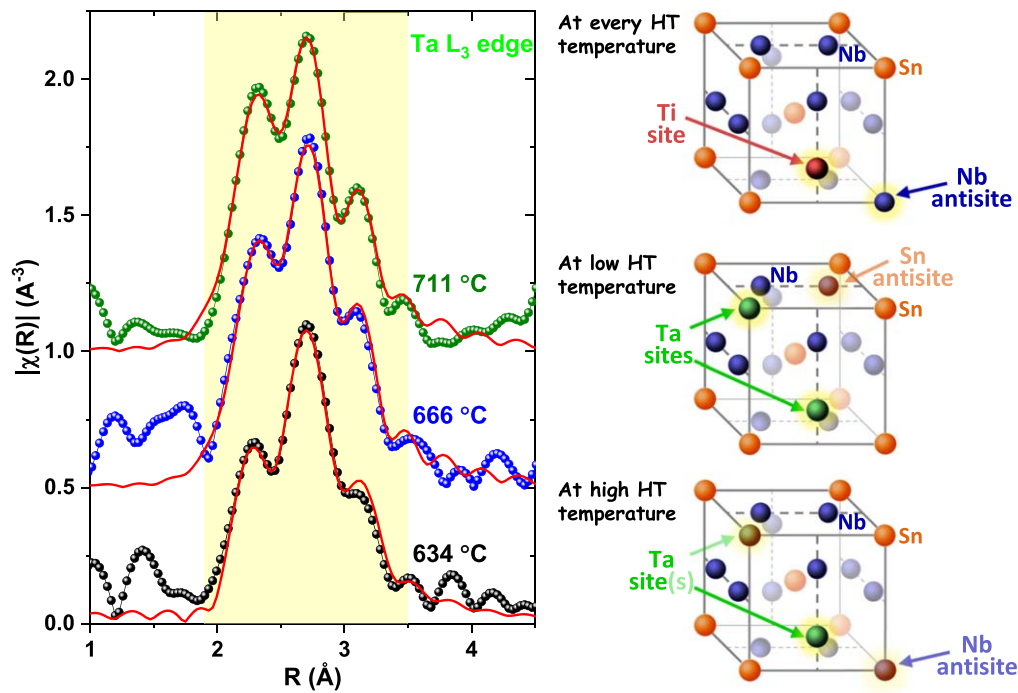


Figure 6. (left) Fourier transforms of the k^2 weighted $\chi(k)$ data for the Ta L_3 edge using the k range 2–11.5 for three differently heat treated Ta-doped RRP[®] samples. The points and line are the data, the red curves are the two-site fits (fitting window of interest for Nb₃Sn from 1.9 to 3.5 Å; the data are not phase corrected). The 666 °C and 711 °C curves are vertically shifted for clarity. (right) Crystalline structure sketches indicate that Ti always occupies the Nb sites, whereas Ta, which is also temperature dependent, splits between the Nb and Sn sites. The main type of antisite disorder that the dopants generate was demonstrated in [23]. The crystalline structure sketches are modified (by removing the indications of the emitting atoms and of the coordination shells and by adding site occupancies) from the Nb₃Sn structure schematic reported by Heald *et al* in the center of figure 1 in [23]. CC BY 4.0.

special alloyed wires, the Kramer plot cannot in any case be used to estimate H_{Irr} because mid-field extrapolation would lead to large overestimations.

3.3. EXAFS characterization of RRP[®] wires

Nb and Sn sites in the A15 structure have different coordination shells [23]. The Nb site has three closely spaced nearest neighbor shells that produce a distinct 3-peak structure in the Fourier-transformed EXAFS spectrum. On the other hand the Sn site only has a single nearest neighbor shell generating a single peak in the Fourier-transformed EXAFS spectrum at the same position of the central peak of Nb three-peak structure [23]. This difference allows us to distinguish on which site the dopant sits. The experiment performed on the series of 5 Ti-doped samples reveal that Ti always sits on the Nb site independent of the HT temperature, similarly to what we previously found on the single HT studied in [23]. Those two studies do agree on there being a strong preference of Ti for the Nb site. In contrast, a quite different behavior was found for the Ta-doped samples. Figure 6 shows the Fourier transformed data for the Ta L_3 edge of the same Ta-doped conductor after different HTs. Despite all samples showing the three-peak structure suggesting that most of the Ta sits on the Nb site, it can be seen that the spectra are changing with the HT reaction. In particular the central peak, which is affected by Ta on both Nb and Sn sites, is decreasing in intensity with respect to the other two peaks that are

produced by Ta occupying the Nb site. The EXAFS data in the main structure range (marked in yellow in figure 6) were fitted using the Artemis software [29] with a model allowing the dopants to occupy either site. The best fits reveal a significant reduction of the Ta concentration on the Sn site with increasing HT temperature. At 634 °C almost half of Ta, $43\% \pm 7\%$, is on the Sn site. At 666 °C and 711 °C the Ta on the Sn site drops to $11\% \pm 4\%$ and $8\% \pm 4\%$, respectively.

3.4. H_{c2} characterization on RRP[®] wires by specific heat

Specific heat characterizations up to 16 T were performed on the Ta-doped RRP[®] wires in order to determine the temperature dependence of H_{c2} , as shown in figure 7 together with the WHH [30] fits and the H_{c2} slope near T_c . The estimated $H_{c2}(0)$ monotonically increases from about 26.7 to 28.1 T with increasing HT temperature.

4. Analysis and discussion

4.1. High-field characterization and H_{Irr}

Our high field results show that the typically used Kramer extrapolation fails to accurately predict H_{Irr} for both standard ternary wires and in newly developed quaternary wires. To evaluate how poor the H_{Irr} estimation is when using the Kramer extrapolations from data limited only to a low or

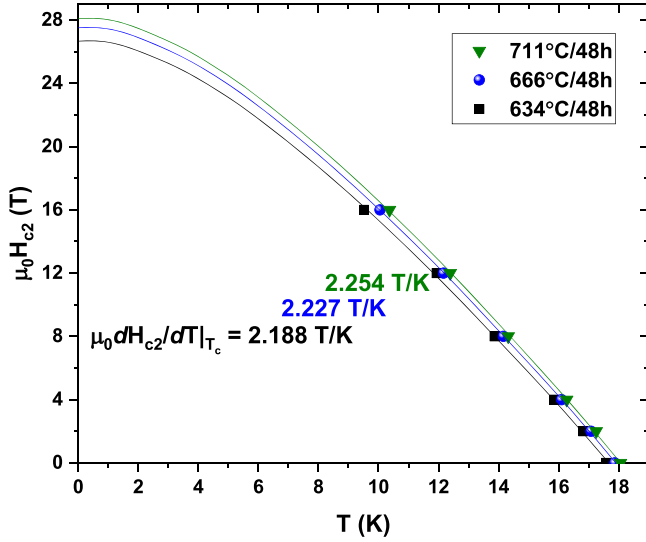


Figure 7. Temperature dependence of H_{c2} for the Ta-doped conductor after three different heat treatments. The lines correspond to the WHH fits for the three cases.

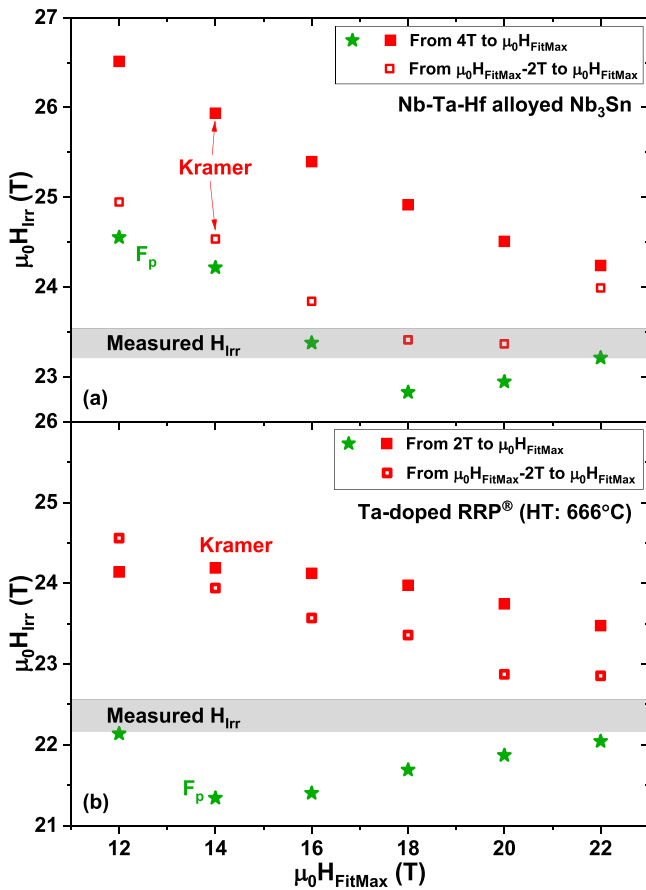


Figure 8. H_{Irr} as a function of the maximum fitting-field ($\mu_0 H_{FitMax}$) estimated from the standard Kramer function (squares) and from the F_p curve fits (stars). Data are at 4.2 K for the Ta–Hf-doped monofilamentary wire (a) and for the Ta-doped RRP[®] wire heat treated at 666 °C (b). The horizontal shaded areas represent the actual H_{Irr} value measured at high-field.

mid-field range, we determined H_{Irr} by linear fits over different field ranges. Figure 8 shows these H_{Irr} estimations as a function of $\mu_0 H_{FitMax}$, the maximum fitting field, to simulate the lack of high field data. We used two fitting ranges for the extrapolation: a wide field range [from 4 T to $\mu_0 H_{FitMax}$ in (a) and from 2 T to $\mu_0 H_{FitMax}$ in (b), which substantially excludes only the low-field data near the Kramer plot maximum] and a 2 T-range below $\mu_0 H_{FitMax}$ [from ($\mu_0 H_{FitMax} - 2$ T) to $\mu_0 H_{FitMax}$]. In both cases, because of the nonlinearity, the Kramer extrapolations over a wide field range (full red squares) strongly overestimate (by several Tesla) the actual H_{Irr} (represented by the grey shadow area), regardless of the fitting range. If we extrapolate using only a 2 T-range below $\mu_0 H_{FitMax}$ (open red squares) the error is in general reduced but, for the RRP wire, the error still remains ~ 0.5 – 2.5 T. A better estimation from a 2 T-range extrapolation can be obtained on the Ta–Hf-doped wire but only with data up to 18 T.

Other approaches can be attempted for a more reliable H_{Irr} estimation from mid-field characterization. As explained earlier, the principal expected pinning mechanisms are by GB (always present) and by PD (in more recent pinning-engineered materials) whose respective F_p field dependences are:

$$F_{p,GB}(H) = A_{GB} \left(\frac{H}{H_{Irr}} \right)^{0.5} \left(1 - \frac{H}{H_{Irr}} \right)^2, \quad (1)$$

$$F_{p,PD}(H) = A_{PD} \left(\frac{H}{H_{Irr}} \right) \left(1 - \frac{H}{H_{Irr}} \right)^2. \quad (2)$$

The generic equation

$$F_p(H) = A \left(\frac{H}{H_{Irr}} \right)^p \left(1 - \frac{H}{H_{Irr}} \right)^q \quad (3)$$

could in principle also be used to estimate H_{Irr} . However, fitting the $F_p(H)$ curve without high-field data can also generate large errors. In figure 8 $F_p(H)$ -fit estimations (green star symbols) are plotted as a function of $\mu_0 H_{FitMax}$. That both negative and positive errors exceeding 1 T occur depending on the fitting range make it clear that this approach is not accurate. It is also important to note that the lack of temperature scaling of the F_p curves implies that the p and q parameters are actually temperature dependent and cannot be assumed constant.

The linearized GB function (equation (1)) is the Kramer function $Kr(H) = J_c^{0.5}(\mu_0 H)^{0.25}$ but a more generalized relation such as $Kr_{\alpha,\beta}(H) = J_c^\alpha(\mu_0 H)^\beta$ can be considered. Varying α and β is equivalent to changing p and q in equation (3), since p and q are related to α and β by the relation $\alpha = 1/q$ and $\beta = (1-p)/q$. However, a simplified case may be usefully considered. In fact a linearization function for PD pinning (equation (2)) assumes the form $Kr_{PD}(H) = J_c^{0.5}(\mu_0 H)^0 = J_c^{0.5}$. So in the case of mixed GB and PD pinning mechanisms, typical of some modern artificial-pin wires, a phenomenologically modified Kramer function could be expressed as $Kr_{\beta}(H) = J_c^{0.5}(\mu_0 H)^\beta$, explicitly varying β to obtain a linear trend. Those mixed GB and PD cases are easily recognizable by a strong downward curvature

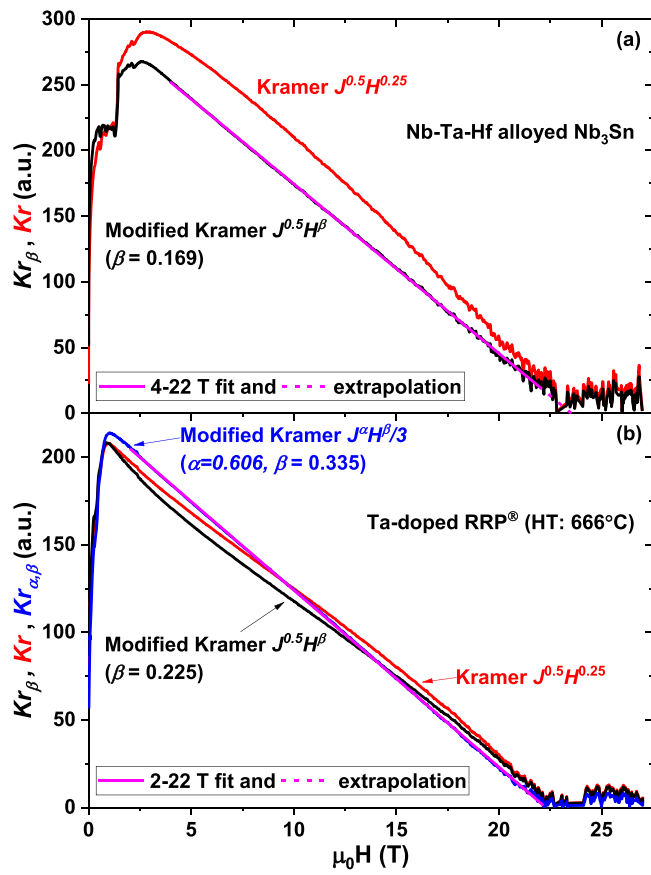


Figure 9. Kramer function and modified Kramer functions at 4.2 K for the Ta–Hf-doped monofilamentary wire (a) and for the Ta-doped RRP[®] wire heat treated at 666 °C (b). The shown modified Kramer functions are the ones obtained by varying α and β (or only β) for the best linear fits in the 4–22 T and 2–22 T ranges (panels (a) and (b), respectively). See text for details.

of the Kramer plot over the entire field range (leading to the strong H_{Irr} overestimation shown in figure 8(a)), like the Ta–Hf case.

In figure 9(a) we apply the $Kr_\beta(H)$ expression to the Ta–Hf sample and compare it to the Kramer function. $Kr_\beta(H)$ generates more consistent H_{Irr} values, within 0.5 T accuracy even when the fitting range is limited to low fields [black circles in figure 10(a)]. Figure 9(a) shows the good linear trend obtained over a wide field range (4–22 T), indicating that this method can be usefully applied to this type of wire with engineered pinning centers even when only mid-field data are available. We attempt the same approach also for the RRP[®] wire [black curve and dots in figures 9(b) and 10(b)] however, varying only β emphasizes the low-field upward curvature mentioned before with the result that the estimated H_{Irr} is only marginally better than the Kramer extrapolation when extending the fit above 18 T. In both samples, determining the best β over a wide fitting-range but extrapolating H_{Irr} only from the 2 T-range below $\mu_0 H_{FitMax}$ (open black circles in figure 10) results in a better estimation but, for the RRP sample, still not better than the similarly obtained Kramer extrapolation.

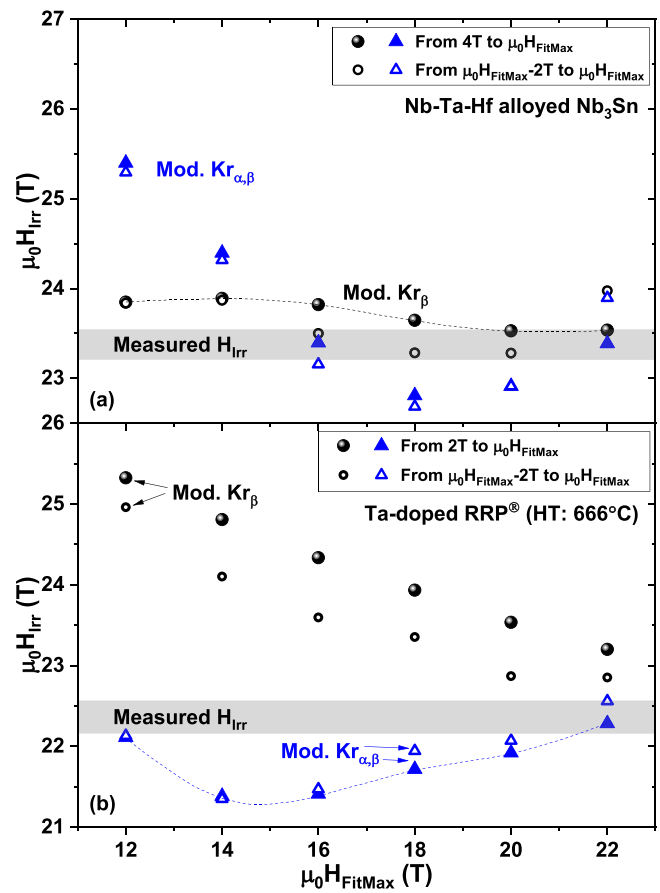


Figure 10. H_{Irr} as a function of the maximum fitting-field ($\mu_0 H_{FitMax}$) estimated from the modified Kramer functions $Kr_\beta(H)$ (circles) and $Kr_{\alpha,\beta}(H)$ (triangles). Data are at 4.2 K for the Ta–Hf-doped monofilamentary wire (a) and for the Ta-doped RRP[®] wire heat treated at 666 °C (b). The horizontal shaded areas represent the actual H_{Irr} value estimated at high-field. See text for details.

Although the most generic $Kr_{\alpha,\beta}(H)$ expression, varying both α and β , can be considered, this does not produce more accurate H_{Irr} estimations for the Ta–Hf sample [blue triangles in figure 10(a) are no better than the F_p estimated ones in figure 8] and only marginally better values are found for the RRP sample [blue curve and triangles in figure 9(b) and 10(b)].

In summary, the results in figures 8–10 show that a reliable estimation of the true H_{Irr} requires using fields well above those typically available in most laboratories. Most importantly, the commonly used Kramer extrapolation from mid-field cannot be used to determine the irreversibility field, since it strongly overestimates the actual H_{Irr} values by 2–3 Tesla. The Kramer extrapolation should thus be considered accurate only in those rare cases where a linear trend can be observed over a wide temperature- and field-range (from just above the Kramer plot maximum up to the maximum available field). The lack of temperature scaling for the F_p curves and the deviation from the Kramer function both at low and high fields clearly differs from what had previously been reported, albeit on different designs of Nb_3Sn conductors [8]. Although the origin of this deviation is unclear, we have also to take into account that most of the previous high-field

characterizations were performed using transport measurements that provide a limited number of data points, and thus can miss small deviations that are more apparent from the almost continuous VSM data reported here. In the case of mixed GB/PD pinning a modified Kramer function of the type $Kr_{\beta}(H) = J_c^{0.5}(\mu_0 H)^{\beta}$ allows a more accurate H_{Irr} estimation, within an 0.5 T error, even with data limited to 12 T; a correct estimation can be obtained with data up to 16 T (from the 2 T-range extrapolation). For more conventional wires, like RRP, $Kr_{\beta}(H)$ does not work well and the more general $Kr_{\alpha,\beta}(H) = J_c^{\alpha}(\mu_0 H)^{\beta}$ expression provides estimates similar to fitting the F_p curve with 4 free parameters with significant variation on the H_{Irr} estimation depending on the maximum field available. This means that in conventional conductors there is no reliable way to determine the true H_{Irr} from mid-field data and high-field characterization is required.

$H_{Irr}(4.2\text{ K})$ was also evaluated at high-fields on the other two Ta-doped RRP samples, revealing a clearly reduced H_{Irr} after the 634 °C HT ($\sim 20.3\text{ T}$) and a mildly suppressed value after the 711 °C HT ($\sim 22.0\text{ T}$) when compared to the $\sim 22.4\text{ T}$ obtained with the 666 °C HT. This implies that the Nb–Ta–Hf alloyed Nb_3Sn does not have a suppressed actual H_{Irr} as was observed in Nb–Zr alloyed Nb_3Sn wire [31, 32]. In fact we measured $\mu_0 H_{Irr}(4.2\text{ K}) \sim 23.4\text{ T}$, about 1 T larger than the best Ta-doped RRP sample studied in this work, making Nb–Ta–Hf alloy a promising material for high-field Nb_3Sn optimization. It is important to note that all the H_{Irr} values estimated in this work are lower than those previously reported for transport on RRP stands [$\mu_0 H_{Irr}(4.2\text{ K}) \geq 24\text{ T}$] [33], however, this is typical of VSM characterizations.

4.2. EXAFS and H_{c2} characterizations

The change of dopant site occupancy by varying HT temperature is a new observation that adds further complexity to the issue of how dopants disorder the A15 structure and raise H_{c2} . In our previous work [23] we postulated that the higher H_{c2} of Ti-doped Nb_3Sn with respect to the Ta-doped Nb_3Sn is that Ti, sitting only on the Nb site, induces more anti-site disorder than the site-splitting Ta. The HT study performed here on the same Ta-doped conductor indicates that Ta site occupancy is variable. Increasing the HT temperature causes the amount of Ta on the Sn site to drop from 43% at 634 °C to 11% at 666 °C and then to only 8% at 711 °C. Thus, Ta behaves at higher temperature more like the Ti dopant in increasing the disorder. Such disorder increase was verified by measuring the temperature dependence of H_{c2} and estimating $d(\mu_0 H_{c2})/dT$ at T_c , which is proportional to the normal state resistivity and so to the disorder. We found that $d(\mu_0 H_{c2})/dT|_{T_c}$ in fact increases from ~ 2.19 , to ~ 2.23 and then to $\sim 2.25\text{ T K}^{-1}$, confirming the increasing disorder associated with sitting Ta on the Nb site (a small increase in T_c was also found). Thus increasing the reaction HT temperature for Ta-doped strands not only improves the chemical homogeneity [25] but also provides the benefits of additional site disorder.

5. Conclusions

This work shows that in Nb_3Sn , despite being one of the most classical superconductors, new measurement techniques and alloys are providing us with a new understanding and suggest that there is the potential for further optimization.

We have previously shown by EXAFS that Ti dopant atoms only occupy the Nb sites in Nb_3Sn whereas Ta splits between Nb and Sn sites; in this study we have shown for the first time that the HT temperature (in the 606–727 °C range) changes the dopant occupancy in the Nb_3Sn structure for Ta but not for Ti. The fraction of Ta on the Sn site drastically decreases when the HT temperature increases from 634 °C to 711 °C. The increasing fraction of Ta atoms on the Nb site introduces more disorder into the structure and can be correlated to an increase in the H_{c2} slope at T_c and, as consequence, a larger H_{c2} at low temperature.

The high field measurements reported here reveal that the pinning force curves taken at different temperatures do not scale (p and q being temperature dependent) and that the Kramer extrapolation is unreliable in all cases investigated, both for conventional large-scale production RRP conductor (both for Ta and for Ti doping) and laboratory-scale Ta–Hf alloyed monofilaments. In the Hf case however, due to the presence of mixed GB and PD pinning mechanisms, a reasonable estimation of H_{Irr} can be obtained with a modified Kramer function of the type $Kr_{\beta}(H) = J_c^{0.5}(\mu_0 H)^{\beta}$ even with data limited to 12 T. In the case of RRP wires, no extrapolation can reliably estimate H_{Irr} and high field characterization over the entire range is necessary. This implies that extensive characterization will be needed for the selection and the HT optimization of conductors for the next generation of higher magnetic field designs. The high-field characterization also revealed that Ta–Hf doped Nb_3Sn presents both a shift in the pinning force maximum and an enhancement of H_{Irr} above the Ta-doped Nb_3Sn values, making this materials of great interest for further development.

Acknowledgments

This work is funded by the US Department of Energy, Office of Science, and Office of High Energy Physics under Award Number DE-SC0012083 and by CERN, and performed under the purview of the US-Magnet Development Program. This work was performed at the National High Magnetic Field Laboratory, which is supported by National Science Foundation Cooperative Agreements NSF DMR-1644779 and by the State of Florida. This research used resources of the Advanced Photon Source, an Office of Science User Facility operated for the US Department of Energy (DOE) Office of Science by Argonne National Laboratory, and was supported by the US DOE under Contract No. DE-AC02-06CH11357, and the Canadian Light Source and its funding partners.

ORCID iDs

Chiara Tarantini  <https://orcid.org/0000-0002-3314-5906>Shreyas Balachandran  <https://orcid.org/0000-0002-0077-8504>Peter J Lee  <https://orcid.org/0000-0002-8849-8995>David C Larbalestier  <https://orcid.org/0000-0001-7098-7208>

References

- [1] Todesco E *et al* 2018 Progress on HL-LHC Nb₃Sn magnets *IEEE Trans. Appl. Supercond.* **28** 1–9
- [2] Chlachidze G *et al* 2017 Performance of the first short model 150 mm-aperture Nb₃Sn quadrupole MQXFS for the high-luminosity LHC Upgrade *IEEE Trans. Appl. Supercond.* **27** 1–5
- [3] Tommasini D *et al* 2018 Status of the 16 T dipole development program for a future hadron collider *IEEE Trans. Appl. Supercond.* **28** 1–5
- [4] Tommasini D *et al* 2017 The 16 T dipole development program for FCC *IEEE Trans. Appl. Supercond.* **27** 4000405
- [5] Scanlan R M, Fietz W A and Koch E F 1975 *J. Appl. Phys.* **46** 2244
- [6] Schauer W and Schelb W 1981 *IEEE Trans. Magn.* **17** 374
- [7] Summers L T, Guinan M W, Miller J R and Hahn P A 1991 A model for the prediction of Nb₃Sn critical current as a function of field, temperature, strain, and radiation damage *IEEE Trans. Magn.* **27** 2041
- [8] Godeke A, ten Haken B, ten Kate H J and Larbalestier D C 2006 A general scaling relation for the critical current density in Nb₃Sn *Supercond. Sci. Technol.* **19** R100–16
- [9] Kramer E J 1973 Scaling laws for flux pinning in hard superconductors *J. Appl. Phys.* **44** 1360
- [10] Ekin J W, Cheggour N, Goodrich L and Splett J 2017 Unified Scaling law for flux pinning in practical superconductors: III. Minimum datasets, core parameters, and application of the extrapolative scaling expression *Supercond. Sci. Technol.* **30** 033005
- [11] Godeke A, Jewell M C, Fischer C M, Squitieri A A, Lee P J and Larbalestier D C 2005 The upper critical field of filamentary Nb₃Sn conductors *J. Appl. Phys.* **97** 093909
- [12] Balachandran S *et al* 2019 Beneficial influence of Hf and Zr additions to Nb₄ at%Ta on the vortex pinning of Nb₃Sn with and without an O source *Supercond. Sci. Technol.* **32** 044006
- [13] Suenaga M 1985 Optimization of Nb₃Sn *IEEE Trans. Magn.* **21** 1122–8
- [14] Rumaner L E, Benz M G and Hall E L 1994 The role of oxygen and zirconium in the formation and growth of Nb₃Sn grains *Metall. Mater. Trans. A* **25** 213–9
- [15] Sekine H, Takeuchi T and Tachikawa K 1981 Studies on the composite processed Nb–Hf/Cu–Sn–Ga high-field superconductors *IEEE Trans. Magn.* **17** 383
- [16] Rumaner L E and Benz M G 1994 Effect of oxygen and zirconium on the growth and superconducting properties of Nb₃Sn *Metall. Mater. Trans. A* **25** 203–12
- [17] Suenaga M, Welch D O, Sabatini R L, Kammerer O F and Okuda S 1986 Superconducting critical temperatures, critical magnetic fields, lattice parameters, and chemical compositions of ‘bulk’ pure and alloyed Nb₃Sn produced by the bronze process *J. Appl. Phys.* **59** 840–53
- [18] Xu X, Rochester J, Peng X, Sumption M and Tomsic M 2019 Ternary Nb₃Sn superconductors with artificial pinning centers and high upper critical fields *Supercond. Sci. Technol.* **32** 02LT01
- [19] Livingston J D 1978 Effect of Ta additions to bronze-processed Nb₃Sn superconductors *IEEE Trans. Magn.* **14** 611
- [20] Tafto J, Suenaga M and Welch D O 1984 Crystal site determination of dilute alloying elements in polycrystalline Nb₃Sn superconductors using a transmission electron microscope *J. Appl. Phys.* **55** 4330
- [21] Heald S M and Tranquada J M 1986 The characterization of cryogenic materials by x-ray absorption methods *Adv. Cryog. Eng. Mater.* 32 (New York: Plenum Press) 471–8
- [22] Flükiger R, Uglietti D, Senatore C and Buta F 2008 Microstructure, composition and critical current density of superconducting Nb₃Sn wires *Cryogenics* **48** 293–307
- [23] Heald S M *et al* 2018 Evidence from EXAFS for different Ta/Ti site occupancy in high critical current density Nb₃Sn superconductor wires *Sci. Rep.* **8** 4798
- [24] Dew-Hughes D 1974 Flux pinning mechanism in type II superconductors *Phil. Mag.* **30** 293–305
- [25] Tarantini C *et al* 2014 Examination of the trade-off between intrinsic and extrinsic properties in the optimization of a modern internal tin Nb₃Sn conductor *Supercond. Sci. Technol.* **27** 065013
- [26] Tarantini C *et al* 2015 Composition and connectivity variability of the A15 phase in PIT Nb₃Sn wires *Supercond. Sci. Technol.* **28** 095001
- [27] Ghosh A K, Sperry E A, D’Ambra J and Cooley L D 2009 Systematic changes of the Nb–Sn reaction with time, temperature, and alloying in restacked-rod-process (RRP) Nb₃Sn strands *IEEE Trans. Appl. Supercond.* **19** 2580
- [28] Tarantini C, Sung Z-H, Lee P J, Ghosh A K and Larbalestier D C 2016 Significant enhancement of compositional and superconducting homogeneity in Ti rather than Ta-doped Nb₃Sn *Appl. Phys. Lett.* **108** 042603
- [29] Ravel B and Newville M 2005 ATHENA, ARTEMIS, HEPHAESTUS: data analysis for x-ray absorption spectroscopy using IFEFFIT *J. Synchrotron Radiat.* **12** 537–41
- [30] Werthamer N R, Helfand E and Hohenberg P C 1966 Temperature and purity dependence of the superconducting critical field, H_{c2} : III. Electron spin and spin-orbital effects *Phys. Rev.* **147** 295
- [31] Xu X, Sumption M D and Peng X 2015 Internally oxidized Nb₃Sn strands with fine grain size and high critical current density *Adv. Mater.* **27** 1346–50
- [32] Motowidlo L R, Lee P J, Tarantini C, Balachandran S, Ghosh A K and Larbalestier D C 2017 An intermetallic powder-in-tube approach to increased flux-pinning in Nb₃Sn by internal oxidation of Zr *Supercond. Sci. Technol.* **31** 014002
- [33] Parrell J A, Field M B, Zhang Y and Hong S 2005 Advances in Nb₃Sn Strand for Fusion and Particle Accelerator Applications *IEEE Trans. Appl. Supercond.* **15** 1200